



Final Draft
of the original manuscript:

Wen, Q.; Li, W.; Patel, V.; Bergmann, L.; Klusemann, B.; dos Santos, J.:
**Assessing the Bonding Interface Characteristics and Mechanical Properties
of Bobbin Tool Friction Stir Welded Dissimilar Aluminum Alloy Joints.**
In: Acta Metallurgica Sinica (English Letters). Vol. 34 (2021) 125 - 134.
First published online by Springer: 08.07.2020

<https://dx.doi.org/10.1007/s40195-020-01101-4>

**Assessing the bonding interface characteristics and mechanical properties of
bobbin tool friction stir welded dissimilar aluminum alloy joints**

Quan Wen ^{1,2}, Wenya Li ^{1 *}, Vivek Patel ¹, Luciano Bergmann ², Benjamin
Klusemann ^{2,3}, Jorge F. dos Santos ²

¹ State Key Laboratory of Solidification Processing, Shaanxi Key Laboratory of Friction Welding Technologies, Northwestern Polytechnical University, Xi'an 710072, Shaanxi, PR China

² Helmholtz-Zentrum Geesthacht, Institute of Materials Research, Materials Mechanics, Solid-State Joining Processes, Geesthacht 21502, Germany

³ Leuphana University of Lüneburg, Institute of Product and Process Innovation, Universitätsallee 1, 21335 Lüneburg, Germany

* Author for correspondence: Tel.: +86-29-88495226, Email: liwy@nwpu.edu.cn
(Wenya Li)

Abstract

This study focuses on the bonding interface characteristics and mechanical properties of the bobbin tool friction stir welded dissimilar AA6056 and AA2219 aluminum alloy joints using different welding speeds. Void defects develop solely in the stir zone at the AA2219 side. A distinct boundary with limited material mixing develops at the middle section of the bonding interface, while excellent material mixing with an irregularly jagged pattern forms at the top and bottom sections of bonding interface. Increasing the welding speed, the material mixing is rarely changed at the middle section in comparison with the bottom section. Furthermore, a small difference between Guinier-Preston (GP) dissolution and Q phase precipitation leads to rare change of hardness in the heat affected zone at the AA6056 side. The increased hardness of the HAZ at the AA2219 side is attributed to avoidance of the dissolution of the θ'' phase precipitates.

A maximum tensile strength of 181 MPa is obtained at 300 mm/min. The fractures occur at the AA6056 side near the top and bottom surfaces, and at the bonding interface in the middle section of the joints. The regions close to the top and bottom surfaces of joints show a better ductility.

Keywords: Bobbin tool friction stir welding; dissimilar aluminum alloy; bonding interface; precipitation; mechanical property

1 Introduction

Bobbin tool friction stir welding (BTFSW) has been developed from friction stir welding (FSW), employing different tool structures and morphologies [1,2]. In BTFSW, the tool consists of a probe and two shoulders, namely the upper and lower shoulders. The upper shoulder serves the same purpose as like in conventional FSW [3,4], while the lower shoulder replaces the backing anvil typically used in FSW. With this arrangement, BTFSW allows to weld the closed or hollow structures. Moreover, the heterogeneous microstructure through the thickness of FSWed joint can be improved by BTFSW. Xu et al. [5] examined the microstructure evolution in FSW and BTFSW using electron backscattering diffraction (EBSD) to find homogeneously refined grains developing throughout the BTFSWed joint thickness compared to the FSWed ones. In spite of this, the FSW joints have better mechanical properties than the BTFSW joints [6], believing that the larger heat input is responsible to the decrease of the joint strength. However, the homogeneously refined grains are favorable to improve corrosion behavior of the joint. As investigated by Esmaily et al. [7], an improved corrosion resistance in BTFSWed joints was achieved as compared to FSWed joints. For lightweight manufacturing, Zhou et al. [8] carried out the BTFSW of AZ61 magnesium alloy, and reported the correlation between mechanical properties and rotational speeds. At the same time, they found a typical region namely band pattern, where the pore

defect formed easily. Based on a coupled Eulerian-Lagrangian numerical model of the BTFSW process developed in our previous study [9], the forming mechanism of the band pattern was illustrated. These investigations mentioned above have provided some insights on the development of BTFSW.

Joining of dissimilar aluminum alloys has gained more attention of researchers due to combining the advantages of different aluminum alloys and controlling the cost. However, there is a big challenge to obtain defect-free welds with good mechanical properties via fusion welding because of the melting and solidification process, especially for joining the 2XXX and 6XXX series aluminum alloys having larger differences in physical and chemical properties [10]. FSW is a solid state welding process without melting issues, showing great potential in joining of dissimilar aluminum alloys [11,12]. The defect-free joints between AA6061 and AA2024 with excellent material mixing were produced via FSW, as reported by Ouyang et al. [13]. Meanwhile, they found that the microstructure exhibits distinct asymmetry characteristics at both sides of the joints. Moradi et al. [14] also confirmed that the different continuous dynamic recrystallization and overall texture intensity are present in this distinct asymmetric microstructure, attributing to the different nature of material mixing of dissimilar aluminum alloys. In order to improve material mixing, the effect of shoulder geometries on the FSW of dissimilar AA5083/AA6351 alloys was studied by Palanivel et al. [15], reporting excellent mechanical strength and material flow produced by full impeller featured shoulder. At the same time, another factor affecting the material mixing, material configuration in FSW of dissimilar aluminum alloy was investigated as well. Yan et al. [16] found that excellent material mixing and joint fatigue properties are produced when Al-Zn-Mg alloy was placed on the advancing side (AS), and it became worse by the contrary material configuration. Recently, Patel et al.

[17] reviewed literature on FSW of dissimilar aluminum alloy joints, among which the development prospects for joining dissimilar aluminum joints are discussed. In summary, a great deal of investigation has been done on the FSW of dissimilar aluminum alloys.

At present, BTFSW of dissimilar aluminum alloys has not been studied extensively as compared to FSW. The AA2219 and AA2195 aluminum alloys have been joined by BTFSW [18,19], where the macroscopic features and microstructure of the joints were investigated. However, the investigated aluminum alloys are from the same alloy series, where the difference in chemical compositions and mechanical properties are limited. In the recent review by Fuse et al. [20], it is stated that BTFSW of dissimilar materials needs further investigation. In the present study, the BTFSW of AA6056-T4 and AA2219-T87 dissimilar aluminum alloys was carried out to analyze the joint formation, bonding interface characteristics and mechanical properties.

2 Experimental procedure

The AA6056-T4 and AA2219-T87 plates with dimensions of 250 mm × 90 mm × 4 mm were selected as the base material (BM) with chemical compositions as listed in Table 1, and placed on the RS and AS, respectively, as shown in Figure 1. The tool is composed of two 15 mm diameter shoulders, i.e. the upper and lower shoulders, and a 7 mm diameter cylindrical probe. The BTFSW without an offset was performed along the longitudinal direction of the plate on a five-axis kinematic robot system (PKM-T805). The gap size between the two shoulders was dominated by a constant gap force of 3300 N. Different welding speeds varying from 300 mm/min to 400 mm/min were used at a constant rotational speed of 500 rpm. The metallographic samples were cut perpendicular to the welding direction, and then etched using BARKER at 24 V for 200 s following polishing. Microstructure characteristics were checked by the optical

microscope (OM) and scanning electron microscope (SEM). Differential scanning calorimetry (DSC) samples were produced as 5mm diameter wafer with 50 mg weight, and then tested on a DSC 200 F3 Maia machine. The temperature cycle was set at rate of 20 °C/min during the heating cycle from 20 °C to 590 °C. The tensile samples were cut perpendicular to the welding direction and prepared according to ASTM-E8E. Tensile tests were performed on a Zwick & Roell machine using a constant crosshead speed of 1 mm/min. Microhardness measurements were performed on Vickers hardness tester (LECO, M-400-H) at a load of 200 g for 10 s. The SEM was used to study the fracture surface of the joints.

3 Results and discussion

3.1 Force and heat input energy variations

Fig. 2a shows the force variations in the welding direction and the torque during BTFSW process for different welding parameters. Both the force and torque increase rapidly at the beginning of the process, where after the run-in time the values slightly decrease with continuous process time. As measured by Goebel et al. [21], the total torque of 50 N·m developing in BTFSW is considerably higher than that in FSW, which increases the risk of pin breakage. Huang et al. [22,23] proposed a novel self-support friction stir welding to prevent pin breakage in BTFSW process. Meanwhile, this method can easily adapt the change in thickness of the plate for simplify welding process [24], providing a new outlook for the development of BTFSW. Later into the process, materials get soften from frictional heat, which results into slight reduction of force and torque. As the welding speed varies from 300 mm/min to 400 mm/min, the force and torque increase from 1300 N to 2200 N, and from 42 N·m to 45 N·m respectively. Therefore, the force in the welding direction is more sensitive to the variation of welding speeds as compared to the torque. Fig. 2b shows the line input

energy (i.e. welding heat input per unit length) change during welding, where the line energy is inversely proportional to welding speed. During welding, the line input energy decreases with increasing welding speed. It is expected that frictional heat gets transferred through conduction, which further softens the material when tool moves to the end position of weld [25], thereby further reducing the resulting line energy.

3.2 Bonding interface characteristics

Cross-sectional micrographs of the joints at various welding speeds are presented in Fig. 3, where it can be seen that the bonding interface at joint shows a linear shape instead of zig-zag feature for all welding parameters. Yan et al. [26] stated that an irregular or wiggly bonding interface in case of dissimilar aluminum alloy joints indicate excellent material flow and mixing. In other words, a linear bonding interface in the present study is associated with a weak material flow, which may be related to the placement of plates rather than the welding parameters. This assumption stems from the fact that the bonding interface shape remains unaffected for the different welding parameters. A sound joint is produced at 300 mm/min, as shown in Fig. 3a. As the welding speed further increases, void defects are formed in the joint. There is a proportional relationship between welding speed and the size of void defect, due to reduced material plasticity at higher welding speeds. It should be noted that all void defects are observed at the SZ of the AA2219 side, close to the thermo-mechanically affected zone (TMAZ). The reason is that AA6056 has lower hardness and yield strength, and higher elongation than that of AA2219. Thus, AA6056 has better plastic formability than AA2219. During welding process, AA6056 adhered to the rotating tool moves from the RS to the AS, and then it is released from the rotating tool. However, it is difficult to embed AA6056 into AA2219 due to their difference in mechanical properties. Thus, the distinct bonding interface is formed. Besides, the restricted

material does not fill the empty region caused by the forward movement of the probe, leaving the void defects at the SZ near AA2219 side.

The microstructures of the typical regions marked in Fig. 3a are shown in Fig. 4. Zone A and B belong to the top and middle sections of the TMAZ of joint on the AS, respectively. As seen in Fig. 4a, the material is deformed plastically by rotating shoulder, producing severely deformed elongated grain. There is a linear bonding interface between the TMAZ and the SZ in the micrograph taken at the middle section (as shown in Fig. 4b), correlating to the limited shear action of the probe. In this region, the grains are less deformed compared to the top section. Figs. 4c and 4d display the bonding interface features at the top and bottom sections within the SZ, respectively. The AA2219 and AA6056 are intermixing together near the upper and lower shoulders, and the bonding interface shows an irregular and jagged pattern due to excellent material mixing. Material flow in BTFSW process shows a dumbbell shaped distribution, with higher shear and stirring velocities formed close to both shoulders instead of probe [9]. Thus, appropriate material flow is predisposed to form near the two shoulders, which facilitates the intermixing of the bonding interfaces.

Fig. 5 shows the bottom and middle sections of bonding interface within the SZ for different welding speeds. With increasing welding speed, the material intermixing at the bottom bonding interface becomes weaker, and a distinct bonding interface boundary is obtained at 400 mm/min. It is correlated to a decrease in stirring intensity per unit length with increased welding speed for a constant rotational speed. In contrast, the middle section of the bonding interface morphology rarely changes as welding speed increases. An irregular wavy bonding interface is developed at the welding speed of 300 mm/min. The distinct bonding interfaces are formed simultaneously at welding speeds of 350 mm/min and 400 mm/min. In summary, the welding speed has a

significant effect on the behavior of the bonding interface near both shoulders. Material flow at the top and bottom sections of bonding interface is stronger than in the middle section, especially for the low welding speed used.

Fig. 6a exhibits the SEM images of the middle section of bonding interface in the SZ, with a complete mixing of the two metals without any defects. Secondary phase particles are found near the bonding interface, with the particle numbers and size on the AA2219 side found larger than on the AA6056 side. Besides, particles with large size still remain though intense stirring in the SZ. From the EDS analysis presented in Fig. 6b, Mg, Cu and Fe elements at the bonding interface fluctuate, which affects the mechanical properties of the joints.

Fig. 7a shows the DSC curves of the heat affected zone (HAZ) on the AA2219 side for different welding speeds. Two obvious exothermic peaks are observed for all welding speeds, which is the θ' phase precipitation at 250-300 °C and the θ phase precipitation at 480-520 °C, respectively. Furthermore, an endothermic peak at 200-250 °C is correlated with the dissolution of the θ'' phase. According to Papazian [27], the precipitate sequence for AA2219 aluminum alloy is summarized as α (SSSS) \rightarrow Guinier-Preston (GP) zones $\rightarrow \theta'' \rightarrow \theta' \rightarrow \theta$, and normally the dissolution of GP zones at 50-200 °C takes precedence over the θ'' dissolution. However, there is no GP zones dissolution detected in this study, similar results reported by Cui et al. [28]. This may be correlating to the different welding techniques and thermal histories employed. In case of the θ'' dissolution, the corresponding endothermic peak area is not affected by the welding speed in the range 300 mm/min to 350 mm/min, but an increase in peak is found at the welding speed of 400 mm/min. This indicates that the HAZ has undergone lower temperature than those reached at 300 mm/min and 350 mm/min, thus avoiding the dissolution of θ'' initially present in the BM during BTFSW process. This is

beneficial to the improvement of hardness at the AA2219 side, as depicted in Fig. 8. The AA6056-T4 aluminum alloy incorporates a massive of GP zones that dissolves during the heating stage, resulting in a large endothermic peak at 200 °C for the BM, as shown in Fig. 7b. An exothermic peak B is found around 250 °C, which is the precipitation of Q phase. Compared with the BM, there is a decrease in the dissolution of GP zones at the HAZ on the AA6056 side, owing to partial dissolution of GP zones during the BTFSW process. As welding speed increased, minor changes in the GP dissolution and the Q phase precipitation are determined, reflecting the minor change in the precipitation phase of the HAZ at the AA6056 side.

3.3 Mechanical properties

The inhomogeneous hardness distributions of the joints for different welding speeds are shown in Fig. 8, with hardness of the AA2219 side being higher than the AA6056 side. The hardness contour shows the typical “W” shape, with low hardness values located at the HAZ of both materials, in which is quite similar to typical FSWed joint [29]. However, the BTFSWed joints have a symmetrical hardness distribution through the thickness direction compared to FSWed joint, as Xu et al. [5] observed. This is the result of the process characteristics, where the lower and upper shoulders rotate at the same speed, producing symmetrical frictional heat and material flow in middle of the joints, and resulting in a homogeneous microstructure [30], properties [31] and even the distribution of residual stresses. Therefore, the symmetrical hardness distributions are found in this study as well. Fig. 9 shows the curves of bonding interface of joints at different welding speeds. In the SZ, the hardness values on the AS are higher than on the RS, due to the different properties between AA2219 and AA6056. There is a sharp change in hardness in the SZ, where there is the bonding interface with decreased value from 135 HV to 95 HV. Meanwhile, the hardness of the SZ rarely changes with

increased welding speed. In case of welding speed of 400 mm/min, an abrupt hardness drop in the SZ at the AA2219 side can be observed. The decreased hardness is attributed to the presence of void defect. The hardness in the HAZ at the AA2219 side remains unaffected between welding speed of 300 mm/min and 350 mm/min, but increases sharply at 400 mm/min due to the remaining θ'' phase (see Fig. 7a). At the AA6056 side, the HAZ hardness is not largely dependent on welding speed, and shows a weaker relationship in comparison with the HAZ of the AA2219 side. The different precipitation phases across the joint (presented in Fig. 7b) are the reasons for the differences in the hardness distributions of both HAZs.

Fig. 10 presents the tensile strength and elongation of the joints as a function of welding speeds. As seen, the tensile strength and elongation decrease with increasing welding speeds. The maximum tensile strength of 181 MPa is obtained at the welding speed of 300 mm/min, which is 40.2% of AA2219 (450 MPa) and 52.6% of AA6056 (330 MPa). The most relevant study on the FSW of dissimilar AA6056/AA2024 alloys was reported by Amancio-Filho et al. [32]. They concluded excellent material mixing with lamellar pattern between AA2024 and AA6056 alloys, and the maximum tensile strength of 246 MPa is 55.8% of AA2024 (440 MPa) and 71.4% of AA6056 (344 MPa), respectively. Therefore, the lower strength of the dissimilar alloys joint is achieved by BTFSW compared with FSWed joint. Similar results were reported by Goetze et al. [33], who believed that the declined strength is mainly correlated to the simpler material mixing patterns of the dissimilar alloys in BTFSW. In the present study, the bonding interface produced with 300 mm/min owns better material mixing than those produced with other welding speeds (see Fig. 5), which is beneficial to the increase of joint strength at 300 mm/min.

Fig. 11 presents the cross-sections of the fracture joints at different welding speeds. As seen, the fractures for all joints occur at the AA6056 side near the top and bottom surface, and at the bonding interface in the mid-thickness of the joints, indicating weaker bonding interface. As mentioned above, excellent material mixing is formed near both surfaces due to the rotating shoulders, which improves the interfacial bonding strength of AA6056 and AA2219 in this region. In contrast, the limited material mixing is formed at the middle position, and becomes the preferred region for crack propagation during tensile test. Fig. 12 shows the SEM morphologies of typical positions marked in Fig. 11. As it can be seen from the images, a large number dimples with small size as well as tearing ridges exist on the fracture surfaces near the top surface (see Figs. 12a and 12c), and the lamellar microstructures without any dimples are formed on the middle position of the joint (see Figs. 12b and 12d). In general, dimple structures are always associated with the good ductility, thus the regions close to the top and bottom surfaces own better ductility than the mid-thickness of joints.

4 Conclusions

In the present study, the dissimilar AA2219 and AA6056 alloys were successfully joined via bobbin tool friction stir welding. The force history during welding, the microstructure evolution and mechanical properties of the joints were investigated in detail. Based on the experimental results, the conclusions are summarized as follows:

- (1) An increase in welding speed leads to an increase of the force in welding direction from 1300 N to 2200 N, and to a decrease of the line energy from 473 KJ/m to 368 KJ/m. Both the force and torque reach their maximum value at the beginning of welding.
- (2) Sound joint is obtained at the welding speed of 300 mm/min. Void defects develop at the SZ of the AA2219 side close to the TMAZ for all further welding speeds. A distinct boundary with no material mixing is developed at the middle sections of the

bonding interface. The top and bottom sections of the bonding interface show an irregular and jagged pattern. With increasing welding speed, the materials intermixing at the bottom bonding interface gradually weaken.

(3) Low hardness is measured at the HAZ of both AA2219 and AA6056 side. As welding speed increases, the different GP dissolution peak and Q phase precipitation lead to the rare change of the HAZ hardness at the AA6056 side, avoiding the dissolution of θ'' initially present in the BM results in an increased HAZ hardness at the AA2219 side.

(4) The maximum tensile strength of 181 MPa is produced at the welding speed of 300 mm/min. The fractures occur at the AA6056 side close to the top and bottom surfaces, and at the bonding interface in the mid-thickness of joints. The regions close to the top and bottom surfaces of the joints show a better ductility.

Acknowledgements:

The author, Quan Wen, is grateful for the support provided by the China Scholarship Council (No. 201806290070) and the author, Wenya Li, thanks the fund by the State Key Laboratory of Solidification Processing in NWPU (No. 2019-QZ-01).

References:

- [1] G.Q. Wang, Y.H. Zhao, Y.Y. Tang, Acta Metall. Sin. (Engl. Lett.) **33**, 13 (2020)
- [2] F.F. Wang, W.Y. Li, J. Shen, Q. Wen, J.F. dos Santos, J. Mater. Sci. Technol. **34**, 135 (2018)
- [3] L. Ma, S.Y. Niu, S.D. Ji, P. Gong, Arch. Metall. Mater. **65**, 307 (2020)
- [4] M. Guan, Y.H. Wang, Y.X. Huang, X. Liu, X.C. Meng, Y.M. Xie, J.C. Li, Mater. Lett. **255**, 126506 (2019)
- [5] W.F. Xu, Y.X. Luo, M.W. Fu, Mater. Charact. **138**, 48 (2018)

- [6] A.L. Lafly, D. Alléhaux, F. Marie, C. Dalle Donne, G. Biallas, *Weld. World* **50**, 98 (2006)
- [7] M. Esmailya, N. Mortazavi, W. Osikowicz, H. Hindsefelt, J.E. Svensson, M. Halvarsson, G.E. Thompson, L.G. Johansson, *Corros. Sci.* **111**, 98 (2016)
- [8] L. Zhou, G.H. Li, G.D. Zha, F.Y. Shu, H.J. Liu, J.C. Feng, *Sci. Technol. Weld. Join.* **23**, 596 (2018)
- [9] Q. Wen, W.Y. Li, Y.J. Gao, J. Yang, F.F. Wang, *Int. J. Adv. Manuf. Technol.* **100**, 2679 (2019)
- [10] X.Q. Liu, H.J. Liu, Yan Yu, *Acta Metall. Sin. (Engl. Lett.)* **33**, 115 (2020)
- [11] X. Feng, S.B. Li, L.N. Tang, H.M. Wang, *Acta Metall. Sin. (Engl. Lett.)* **33**, 30 (2020)
- [12] B. He, L. Cui, D.P. Wang, H.J. Li, C.X. Li, *Acta Metall. Sin. (Engl. Lett.)* **33**, 135 (2020)
- [13] J.H. Ouyang and R. Kovacevic, *J. Mater. Eng. Perform.* **11**, 51 (2002)
- [14] M.M. Moradi, H.J. Aval, R. Jamaati, S. Amirkhanlou, S.X. Ji, *J. Manuf. Process.* **32**, 1 (2018)
- [15] R. Palanivel, R. Laubscher, S. Vigneshwaran, I. Dinaharan, *Proc. Inst. Mech. Eng. Part B: J. Eng. Manuf.* **232**, 1384 (2016)
- [16] Z.J. Yan, X.S. Liu, H.Y. Fang, *Acta Metall. Sin. (Engl. Lett.)* **29**, 1161 (2016)
- [17] V. Patel, W.Y. Li, G.Q. Wang, F.F. Wang, A. Vairis, P.L. Niu, *Metals*. **9**, 270 (2019)
- [18] M. Skinner, R.L. Edwards, *Mater. Sci. Forum.* **426-432**, 2849 (2003)
- [19] D.E. Taylor, Dissertation, Louisiana State University, 2009
- [20] K. Fuse, V. Badheka, *Sci. Technol. Weld. Join.* **24**, 277 (2019)
- [21] J. Goebel, M. Reimann, J.F. dos Santos, *J. Mater. Eng. Perform.* **27**, 5212 (2018)
- [22] Y.X. Huang, L. Wan, S.X. Lv, J.C. Feng, *Sci. Technol. Weld. Join.* **18**, 239 (2013)

- [23] Y.X. Huang, L. Wan, T.F. Huang, Z.L. Lv, L. Zhou, J.C. Feng, *Int. J. Adv. Manuf. Technol.* **87**, 1067 (2016)
- [24] L. Wan, Y.X. Huang, W.Q. Guo, S.X. Lv, J.C. Feng, *J. Mater. Sci. Technol.* **30**, 1243 (2014)
- [25] S.D. Ji, Y.Y. Jin, Y.M. Yue, S.S. Gao, Y.X. Huang, L. Wang, *J. Mater. Sci. Technol.* **29**, 955 (2013)
- [26] Z. Yan, X. Liu, H. Fang, *J. Mater. Sci. Technol.* **32**, 1378 (2016)
- [27] J.M. Papazian, *Metall. Trans. A* **12A**, 269 (1981)
- [28] L. Cui, P. Lu, W.K. Li, H.M. Wang, D.P. Wang, Z.P. Zhang, J.L. Song, *Sci. Technol. Weld. Join.* **24**, 27 (2019)
- [29] H.J. Zhang, M. Wang, X. Zhang, G. Yang, *Mater. Des.* **65**, 559 (2015)
- [30] J.J. Shen, F.F. Wang, U.F.H. Suhuddin, S.Y. Hu, W.Y. Li, J.F. dos Santos, *Metall. Mater. Trans. A* **46**, 2809 (2015)
- [31] J.H. Dong, C. Gao, Y. Lu, J. Han, X.D. Jiao, Z.X. Zhu, *Int. J. Miner Metall. Mater.* **24**, 171 (2017)
- [32] S.T. Amancio-Filho, S. Sheikhi, J.F. dos Santos, C. Bolfarini, *J. Mater. Process. Technol.* **206**, 132 (2008)
- [33] P. Goetze, M. Kopyściański, C. Hamilton, S. Dymek, in *Friction Stir Welding and Processing X*, ed. by Y. Hovanski, R. Mishra, Y. Sato, P. Upadhyay, D. Yan (Springer, Nature Switzerland AG, 2019), p. 3

Table and figure captions

Table 1 Chemical compositions of the AA6056 and AA2219 plates (wt%)

AA6056-T4	Al	Mg	Si	Cu	Mn	Fe
	Bal.	0.73	0.87	0.67	0.62	0.12

AA2219-	Al	Cu	Mn	Ti	Zr	Si
T87	Bal.	6.38	0.32	0.06	0.18	0.08

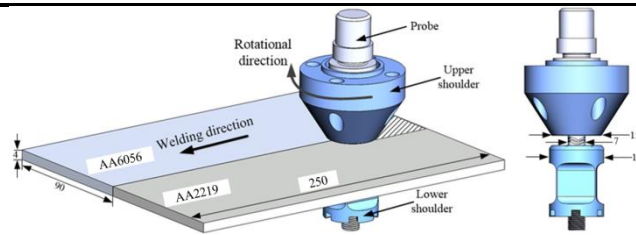


Fig. 1 BTFSW process of dissimilar aluminum alloys

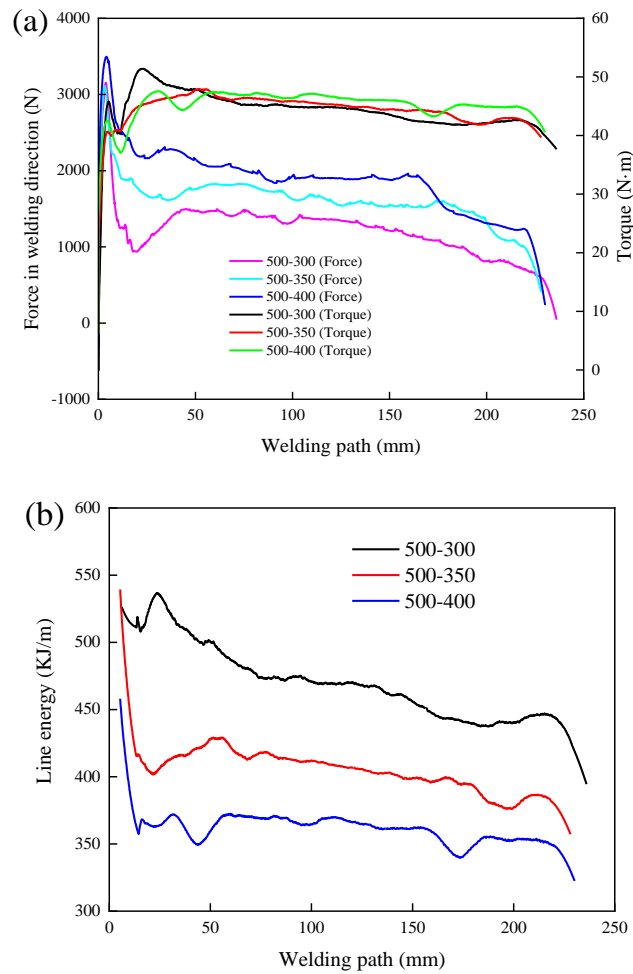


Fig. 2 Variations of (a) the force in the welding direction and torque, and (b) line energy for different welding parameters

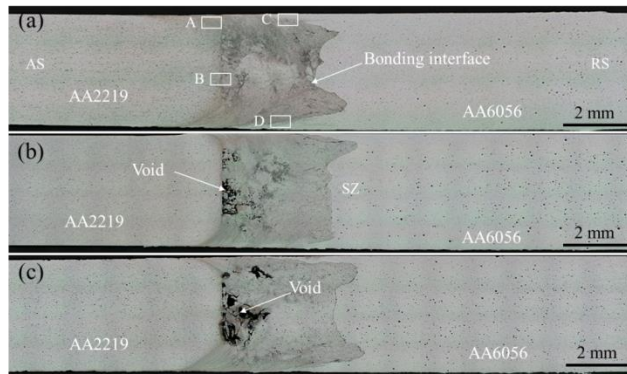


Fig. 3 Macrographs of the BTFSWed joints with different welding speeds; (a) 300 mm/min, (b) 350 mm/min and (c) 400 mm/min

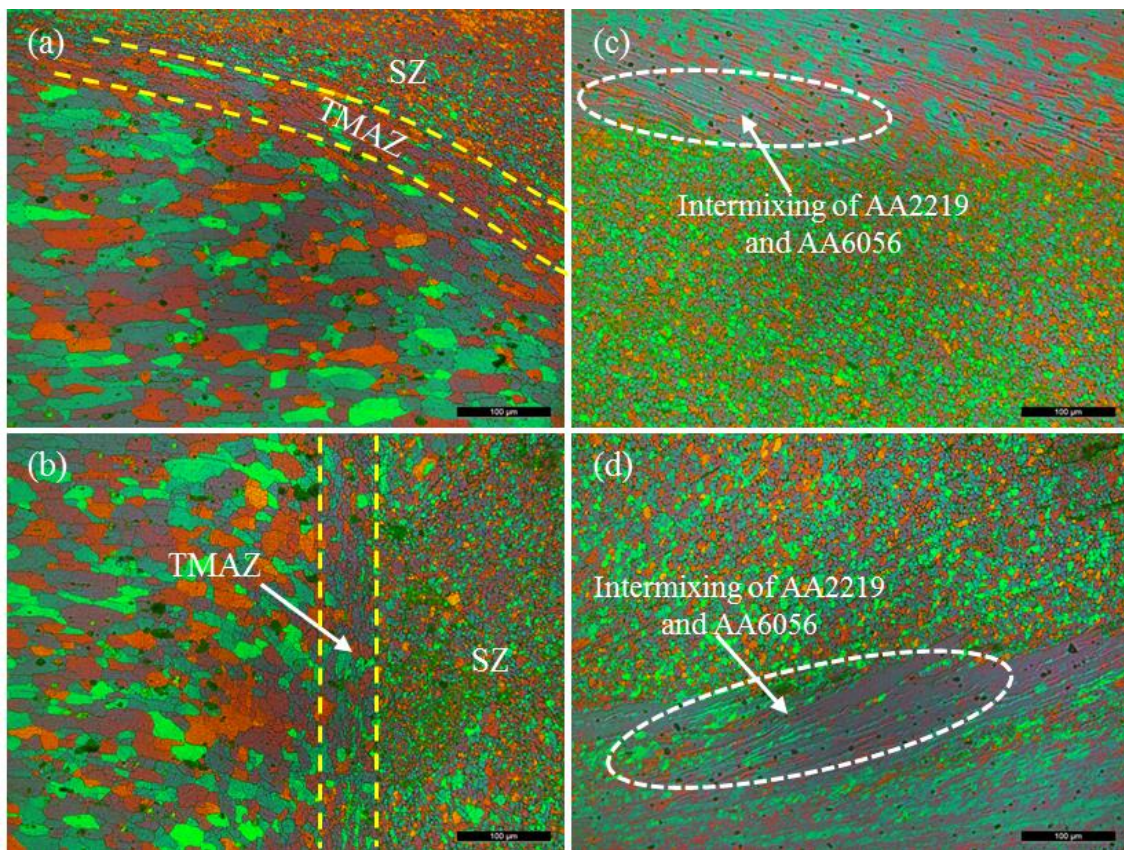


Fig. 4 Microstructure of the different zones marked in fig. 3a (a) zone A; (d) zone B; (e) zone C and (f) zone D

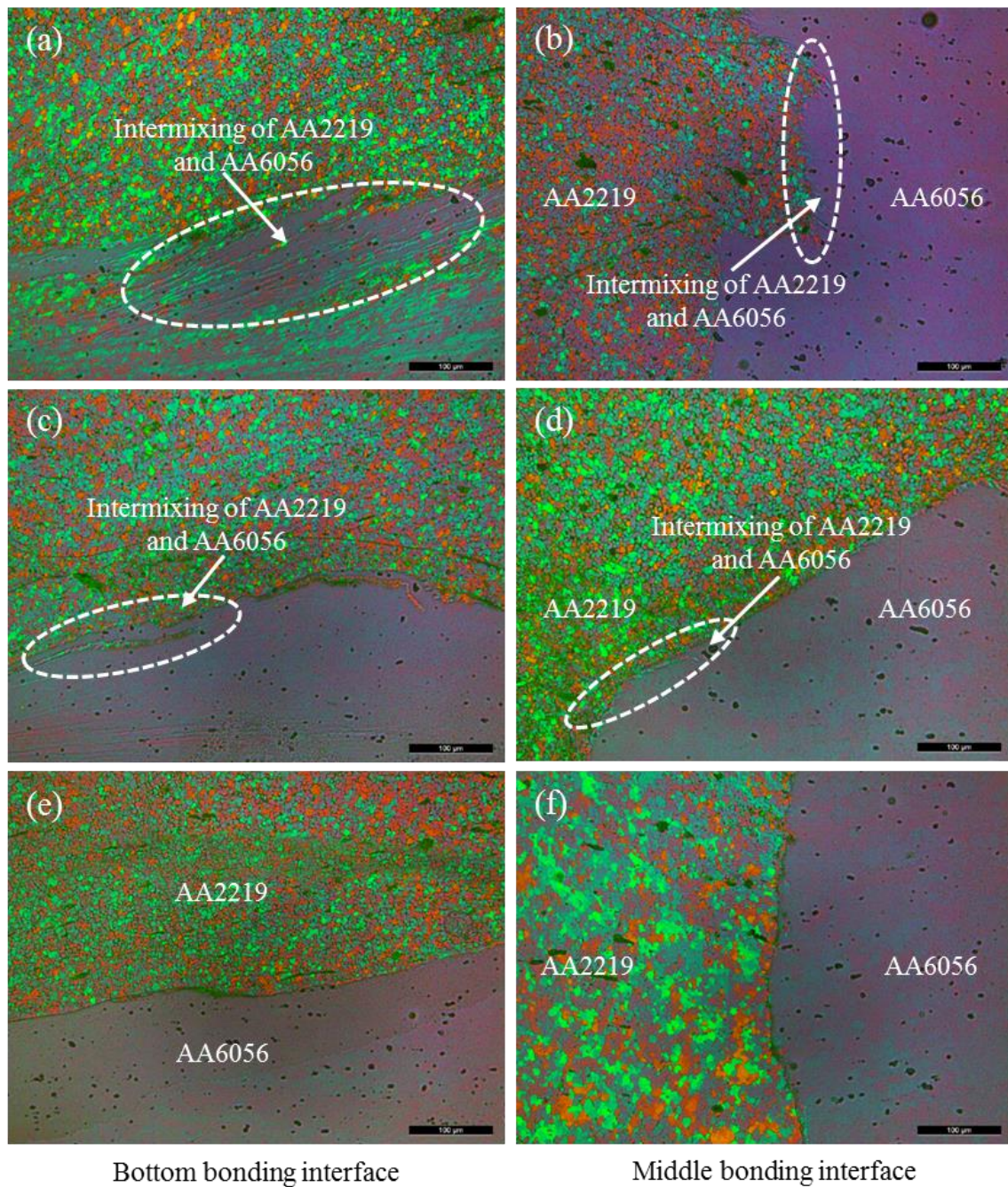


Fig. 5 Bottom and middle sections of bonding interface of the joints welded at different welding speeds of (a,b) 300mm/min (c,d) 350mm/min and (e,f) 400mm/min

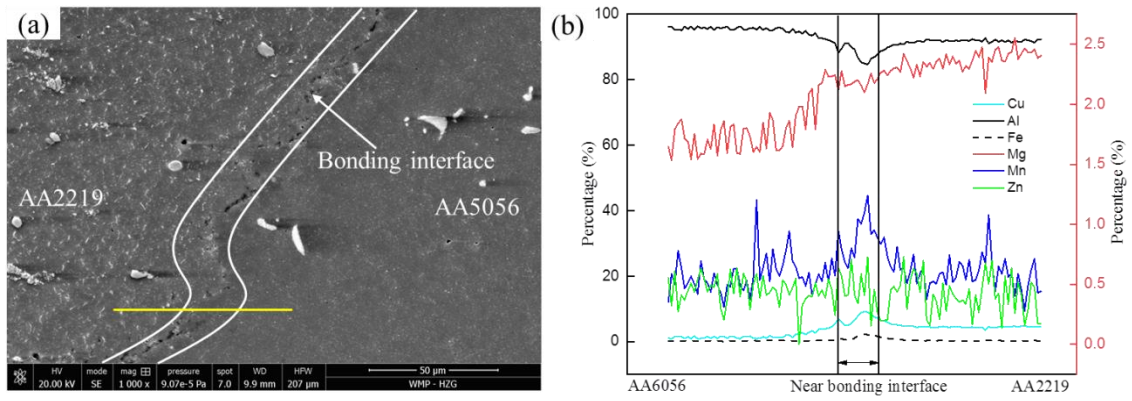


Fig. 6 (a) Bonding interface of the joint obtained at 300mm/min; EDS analysis of (b) the bonding interface

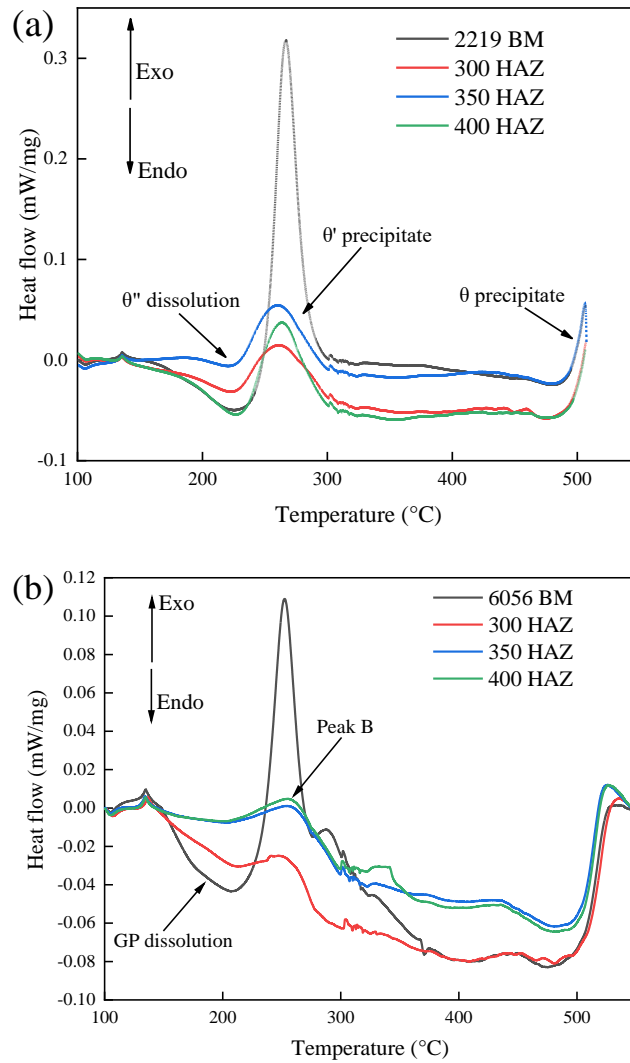


Fig. 7 DSC curves of the BM and HAZ (a) at the AA2219 side and (b) AA6056 side for different welding speeds

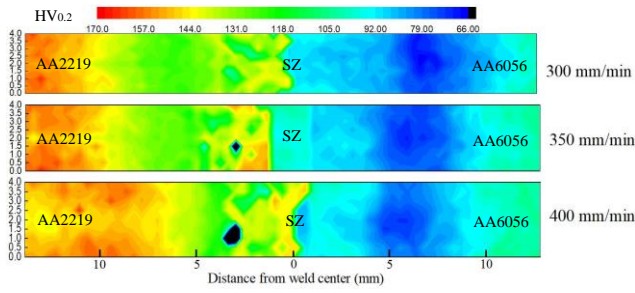


Fig. 8 Hardness maps across the cross-section of the joints at different welding speeds

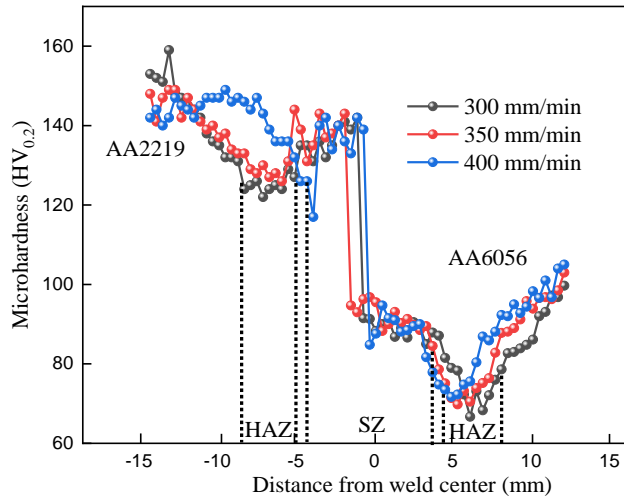


Fig. 9 Hardness curves of bonding interface at the weld center for different welding speeds

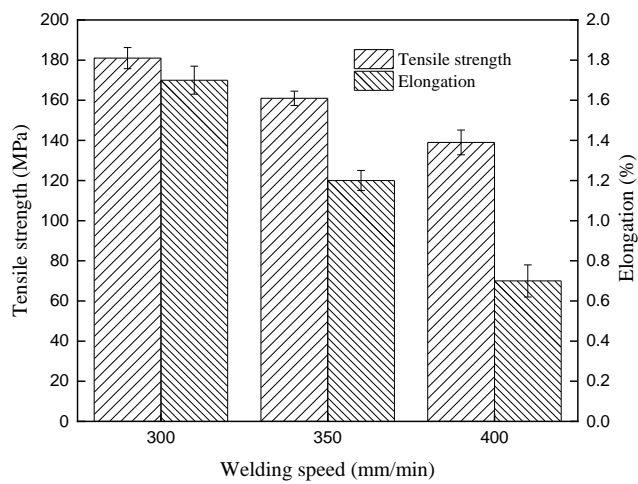


Fig. 10 Tensile strength and elongation at different welding speeds

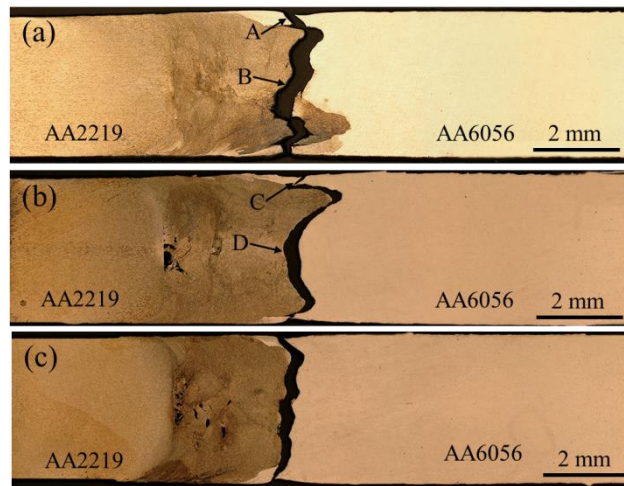


Fig. 11 Cross-sections of the fracture joints welded at different welding speeds: (a) 300mm/min, (b) 350mm/min and (c) 400mm/min

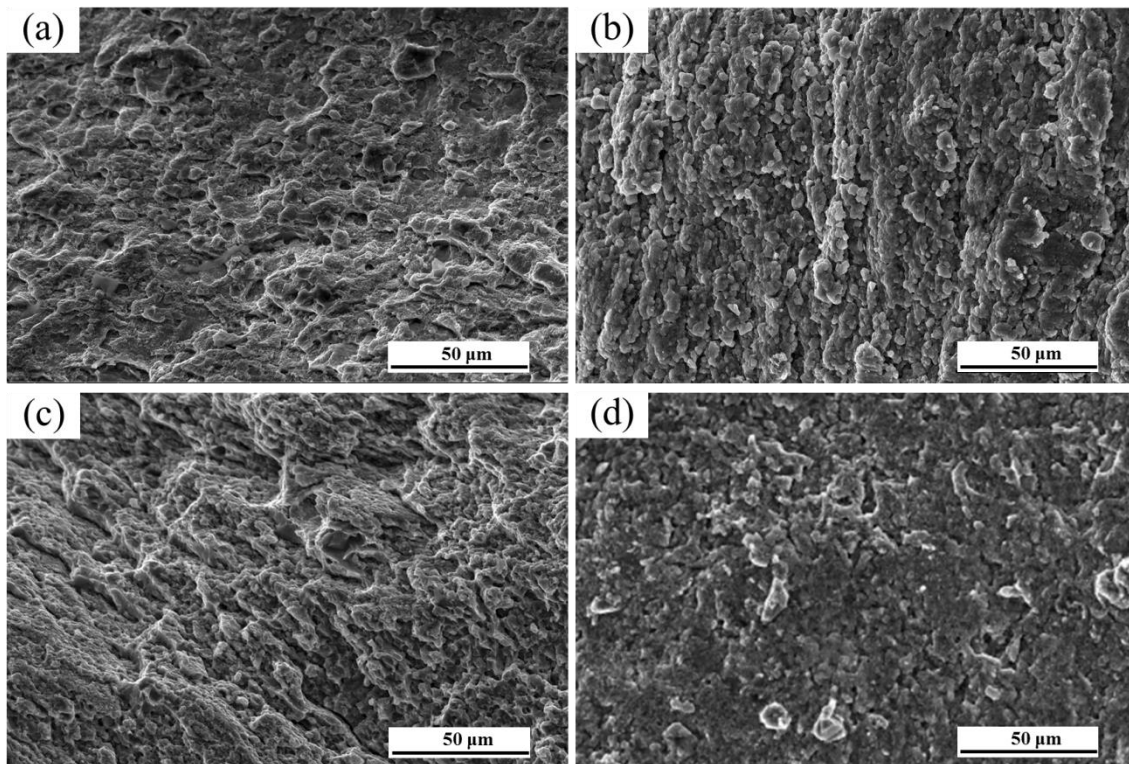


Fig. 12 SEM morphology of typical positions in the tensile fracture joint (a) zone A, (b) zone B, (c) zone C and (d) zone D